Available online at www.sciencedirect.com
SCIENCE DIRECT®
Journal of Sound and Vibration 289 (2006) 450–480
JOURNAL OF SOUND AND VIBRATION
www.elsevier.com/locate/jsvi

Buckling and free vibration analysis of functionally graded cylindrical shells subjected to a temperature-specified boundary condition

Ravikiran Kadoli*, N. Ganesan

Machine Dynamics Laboratory, Applied Mechanics Department, Indian Institute of Technology Madras, Chennai 600 036, India

Received 4 February 2004; received in revised form 16 January 2005; accepted 8 February 2005
Available online 2 June 2005

Abstract

Linear thermal buckling and free vibration analysis are presented for functionally graded cylindrical shells with clamped–clamped boundary condition based on temperature-dependent material properties. The material properties of functionally graded materials (FGM) shell are assumed to vary smoothly and continuously across the thickness. With high-temperature specified on the inner surface of the FGM shell and outer surface at ambient temperature, 1D heat conduction equation along the thickness of the shell is applied to determine the temperature distribution; thereby, the material properties based on temperature distribution are made available for thermal buckling and free vibration analysis. First-order shear deformation theory along with Fourier series expansion of the displacement variables in the circumferential direction are used to model the FGM shell. Numerical studies involved the understanding of the influence of the power-law index, r/h and l/r ratios on the critical buckling temperature. Free vibration studies of FGM shells under elevated temperature show that the fall in natural frequency is very drastic for the mode corresponding to the lowest natural frequency when compared to the lowest buckling temperature mode.

*Corresponding author. National Institute of Technology Karnataka, Mechanical Engineering Department, Surathkal, Srinivasnagar 575025, India. Tel.: +91 824 2474000 (3658); fax: +91 824 2476090.
E-mail address: rkkadoli@nitk.ac.in (R. Kadoli).

0022-460X/$ - see front matter © 2005 Elsevier Ltd. All rights reserved.
doi:10.1016/j.jsv.2005.02.034

1. Introduction

The concept of functionally graded materials (FGMs) was first introduced by a group of Japanese materials scientists in the area of Sendai. Many familiar FGMs are compositionally graded from a refractory ceramic to a metal so that it can incorporate incompatible functions such as the heat, wear and oxidation resistance of ceramics and the high toughness, high strength, machinability and bonding capability of metals without severe internal thermal stress. An in-depth discussion on various issues related to FGMs on modeling aspects to determine the magnitude of thermal stresses that develop due to large thermal loading, the optimal composition of the constituents or the composition profile that helps to decrease the magnitude of thermal stress, formation of cracks and eventually failure of the structural member by fracture and many other topics can be found in the article by Noda [1]. Fuchiyama and Noda [2] have developed a computer program to analyze the transient heat transfer and the transient thermal stresses in FGM components by the finite element method. Obata and Noda [3] have attempted studies to design an optimum functionally graded hollow cylinder and hollow sphere in terms of reducing the thermal stresses due to uniform temperature rise and given the temperature difference between the inside and the outside. Reddy and Chin [4] have developed a coupled as well as an uncoupled thermoelastic finite element formulation to analyze the thermomechanical behavior of functionally graded cylinders and plates subjected to abrupt thermal loading. Jabbari et al. [5] derived Navier's equation for an FGM hollow cylinder taking into account the 1D steady-state heat conduction. Awaji and Sivakumar [6] numerically analyzed the steady-state and transient temperature distributions and related thermal stress distribution in the FGM cylinder composed of mullite-molybdenum system. Takezono et al. [7] carried out numerical studies on the functionally graded cylindrical shells containing hot fluid. Ye et al. [8] discussed a 2D axisymmetric thermoelastic problem of a functionally graded transversely isotropic cylindrical shell. Liew et al. [9] detailed the derivation of an analytical model to carry out studies on functionally graded hollow cylinders subjected to an arbitrary steady-state and transient temperature field. Cho and Ha [10] and Ootao et al. [11] have carried out studies on volume fraction optimization for minimizing thermal stresses in FGMs.

Studies were reported on the application of piezoelectric actuator and sensor for FGM beams, plates and shells for the active shape control and active vibration suppression operating under ambient temperature as well as subjected to temperature gradient by He et al. [12], Ng et al. [13], Liew et al. [14–16]. Formulation and theoretical analysis on topics like postbuckling of FGM plates bonded with piezoelectric materials under combined thermal, electric and mechanical load, nonlinear vibration, large amplitude vibration of initially stressed and parametric resonance of FGM-laminated plates were presented by Liew et al. [17], Kitipornchai et al. [18], Yang et al. [19,20].

Shahsiah and Eslami [21] used Sanders nonlinear strain–displacement relation and first-order shell theory to derive the equilibrium and stability equations for a functionally graded cylindrical shell. Nonlinear postbuckling analysis of functionally graded cylindrical shells was presented by Shen [22] based on the classical shell theory with von-Karman–Donnell type of kinematic nonlinearity. Similarly, based on the classical shell theory including the von Karman–Donnell-type kinematic nonlinearity, Shen [23] considers the study on postbuckling of pressure-loaded FGM cylindrical shells under constant thermal load.

Loy et al. [24] and Pradhan et al. [25] have investigated the vibration behavior of functionally graded cylindrical shells based on Love's theory and the Rayleigh–Ritz method. Their studies

revealed that the frequency characteristics of functionally graded cylindrical shells are similar to those of isotropic shells.

In the case of FGMs the material properties at any point in the component are decided by the volume fraction of the metal or ceramic as well as the characteristics variation chosen for the volume fraction. FGM components are called upon to operate where severe temperature fluctuations exist. These two aspects on FGM necessitates taking into account temperature-dependent material properties. The results obtained from the computation of thermal stresses, thermal transient response and thermal buckling analysis based on temperature-dependent material properties can be entirely different from that obtained based on temperature-independent material properties. Thermal buckling studies of FGM cylindrical shells, which take into account temperature-dependent material properties, are very less in number in the literature. Further, note that elaborate studies, which consider temperature distribution based on the temperature-dependent material property, given the temperature boundary conditions, and subsequently considering the thermal loading to compute initial stresses and hence solving the linear thermal stability problem using semi-analytical finite element method are not reported in the literature. The iterative procedure described by Chen and Chen [26] for computing material properties dependent on temperature distribution for the evaluation of thermal buckling temperature is followed. With this in view the objectives of the present work are as follows: (i) Based on the availability of material properties for metal and ceramic, a combination of ceramic and metal is proposed for FGM shells and the critical buckling temperatures (or bifurcation buckling temperature) are evaluated. Influences of the material combination, variation of the power-law index, length-to-radius ratio and radius-to-thickness ratio on the critical thermal buckling temperature are examined. These studies will provide information for a better combination of metal and ceramic for FGM shell and also the magnitude of power-law index required for better thermal buckling characteristics. (ii) Effect of temperature on the free vibration natural frequencies of FGM cylindrical shells with a temperature gradient across the FGM shell wall.

2. Theoretical formulation

2.1. Material properties definition for functionally graded shells

The present study considers functionally graded material composed of metal and ceramic. The grading is taken into account across the thickness of the shell (i.e. in the radial direction). The literature reveals two approaches to evaluate the material properties of FGM. One approach considers the smooth and continuous variation of the volume fraction of either ceramic or metal based on the power-law index and this approach is widely used by many researchers. The other approach uses the pore distribution as well as volume fraction to evaluate the material properties (Refs. [1–3]). The present work assumes no pores and to start with, a simple power-law-type definition for the volume fraction of the metal, V_f, across the radial direction of the shell is assumed. This is defined as

$$V_f = \left(\frac{r_z - r_i}{r_o - r_i}\right)^{\underline{n}}, \tag{1}$$

where r_z represents radius at any point along the radial direction of the shell, r_i is the inner radius, r_o the outer radius of the shell and $\underline{n}$ the power-law index. Based on the above definition it follows that the inner surface of the cylindrical shell will be ceramic rich. The above definition and other definitions to follow are available in many of the published literature (Ref. [4]). The sum total volume of the constituent materials, ceramic (c) and metal (f), should be

$$V_c + V_f = 1. \tag{2}$$

Composite materials models can be suitably used to predict thermomechanical properties of FGM for a given data of constituent phases (ceramic and metal). There are five basic composite models viz., law of mixtures, shear lag, laminated plate, Eshelby's and variational principle models. Among these, the simplest is the law of mixtures originally proposed by Voigt (Ref. [27]). This simple model provides a reasonably accurate prediction of the mechanical as well as thermal properties of inhomogeneous materials. Based on the volume fraction definition (Eq. (1)) and law of mixtures (Eq. (2)), the effective material property definition follows:

$$(\mathrm{MP})_{\mathrm{eff}} = (\mathrm{MP})_{\mathrm{ot}} V_f + (\mathrm{MP})_{\mathrm{in}} V_c, \tag{3}$$

where 'MP' is the notation for the material property in general. $(\mathrm{MP})_{\mathrm{ot}}$ and $(\mathrm{MP})_{\mathrm{in}}$ represent material properties at outer and inner surfaces of the shell. Making use of Eqs. (1)–(3) the definitions of effective mechanical properties (viz. Young's Modulus E_{eff}, Poisson's ratio v_{eff} and density ρ_{eff}) and thermal properties (thermal conductivity k_{eff} and coefficient of thermal expansion α_{eff}) can be written as

$$E_{\mathrm{eff}} = (E_{\mathrm{ot}} - E_{\mathrm{in}})\left(\frac{r_z - r_i}{r_o - r_i}\right)^{\underline{n}} + E_{\mathrm{in}}, \tag{4a}$$

$$v_{\mathrm{eff}} = (v_{\mathrm{ot}} - v_{\mathrm{in}})\left(\frac{r_z - r_i}{r_o - r_i}\right)^{\underline{n}} + v_{\mathrm{in}}, \tag{4b}$$

$$\rho_{\mathrm{eff}} = (\rho_{\mathrm{ot}} - \rho_{\mathrm{in}})\left(\frac{r_z - r_i}{r_o - r_i}\right)^{\underline{n}} + \rho_{\mathrm{in}}, \tag{4c}$$

$$k_{\mathrm{eff}} = (k_{\mathrm{ot}} - k_{\mathrm{in}})\left(\frac{r_z - r_i}{r_o - r_i}\right)^{\underline{n}} + k_{\mathrm{in}}, \tag{4d}$$

$$\alpha_{\mathrm{eff}} = (\alpha_{\mathrm{ot}} - \alpha_{\mathrm{in}})\left(\frac{r_z - r_i}{r_o - r_i}\right)^{\underline{n}} + \alpha_{\mathrm{in}}. \tag{4e}$$

In the above equations (4a–4e), the subscript '*ot*' stands for the outer surface and '*in*' stands for the inner surface of the cylindrical shell. In addition to the variation of material properties in the radial direction based on the power-law index, it is also possible to consider the above definitions of material properties as a function of temperature. Based on the temperature coefficients the temperature-dependent material properties are evaluated as follows:

$$\mathrm{MP} = P_o(P_{-1}\hat{T}^{-1} + 1 + P_1\hat{T} + P_2\hat{T}^2 + P_3\hat{T}^3). \tag{5}$$

The above equation is a cubic fit for the material property (MP) as a function of temperature and P_{-1}, P_1, P_2 and P_3 are coefficients of temperature $\hat{T}^{-1}$, $\hat{T}$, $\hat{T}^2$ and $\hat{T}^3$, respectively, obtained after factoring out P_o from the cubic curve fit of the property (Ref. [36]). P_o, P_{-1}, P_1, P_2 and P_3 are unique to a particular material. $\hat{T}$ represents the absolute temperature in Kelvin. Thus, the effective material properties of Eq. (3) can truly be represented as a function of thickness as well as temperature:

$$\mathrm{MP}_{\mathrm{eff}}(\hat{T}, z) = \mathrm{MP}_f(\hat{T})V_f(z) + \mathrm{MP}_c(\hat{T})V_c(z). \tag{6}$$

The temperature coefficients for various metals: stainless-steel SUS304, nickel, Ti-6Al–4V, and ceramics: zirconia (ZrO_2), alumina (Al_2O_3), and silicon nitride (Si_3N_4), are obtained from Reddy and Chin [4]. Due to lack of space the material data will not be mentioned in this article.

2.2. Semianalytical finite element formulation for functionally graded shells

The stress–strain relation for a generally isotropic material including the temperature effects based on first-order shear deformation is given by

$$\begin{Bmatrix} \sigma_{ss} \\ \sigma_{\theta\theta} \\ \tau_{s\theta} \\ \tau_{sz} \\ \tau_{\theta z} \end{Bmatrix} = \begin{bmatrix} Q_{11} & Q_{12} & 0 & 0 & 0 \\ Q_{12} & Q_{22} & 0 & 0 & 0 \\ 0 & 0 & Q_{66} & 0 & 0 \\ 0 & 0 & 0 & Q_{44} & 0 \\ 0 & 0 & 0 & 0 & Q_{55} \end{bmatrix} \left(\begin{Bmatrix} \varepsilon_{ss} \\ \varepsilon_{\theta\theta} \\ \gamma_{s\theta} \\ \gamma_{sz} \\ \gamma_{\theta z} \end{Bmatrix} - \begin{Bmatrix} \alpha_{ss}\Delta T \\ \alpha_{\theta\theta}\Delta T \\ 0 \\ 0 \\ 0 \end{Bmatrix} \right), \tag{7}$$

where σ_{ss} and $\sigma_{\theta\theta}$ are the normal stresses, in-plane shear stress is $\tau_{s\theta}$, τ_{sz} and $\tau_{\theta z}$ the thickness shear stresses, ε_{ss} and $\varepsilon_{\theta\theta}$ the normal strains, $\gamma_{s\theta}$ the in-plane shear strain and γ_{sz} and $\gamma_{\theta z}$ the thickness shear strains. The coefficient of thermal expansion in the two principle directions (s, θ) are α_{ss} and $\alpha_{\theta\theta}$. ΔT is the temperature change from a stress-free state. The suffixes used are based on the coordinate system, (s, θ, z), for the shell mid-surface. The stiffness coefficients are defined according to

$$Q_{11} = Q_{22} = \frac{E_{\mathrm{eff}}}{1 - \nu_{\mathrm{eff}}^2}, \quad Q_{12} = \frac{\nu_{\mathrm{eff}} E_{\mathrm{eff}}}{1 - \nu_{\mathrm{eff}}^2}, \quad Q_{44} = Q_{55} = Q_{66} = \frac{E_{\mathrm{eff}}}{2(1 + \nu_{\mathrm{eff}})}. \tag{8}$$

For a given power-law index, the effective Young's modulus E_{eff}, Eq. (4a), and effective Poisson's ratio ν_{eff}, Eq. (4b), need to be evaluated in order to obtain the elastic coefficients Q_{ij}. Banks-Sills et al. [28] discussed the advantages and disadvantages of five functionally graded architectures for dynamic analysis. It was concluded that either the layered model or continuous model is a good approach to study FGM. Similarly, Tanigawa [29] indicated that it is reasonable to consider an FGM shell to be composed of many layers. Each layer can be conceived as a homogeneous layer and follows the definition of the effective material properties as described in Eqs. (4a)–(4e). The semianalytical finite element formulation for the stiffness matrix, mass matrix, evaluation of the thermal load vector, initial stress resultants and moment resultants and finally the initial stiffness matrix is similar to the one discussed in Ganesan and Kadoli [30]. The methodology for the computation of the reduced stiffness coefficients is incorporated into the semianalytical finite

element formulation to compute the stiffness matrix. Rewriting Eq. (7) by neglecting the temperature effects and, the stress–strain relation for a general shell of revolution based on the first-order shear deformation theory is as follows:

$$\begin{Bmatrix} \sigma_{ss} \\ \sigma_{\theta\theta} \\ \tau_{s\theta} \\ \tau_{sz} \\ \tau_{\theta z} \end{Bmatrix}_{i\text{lay}} = [Q]_{i\text{lay}} \left(\begin{Bmatrix} \frac{1}{A_1}\varepsilon^o_{ss} \\ \frac{1}{A_2}\varepsilon^o_{\theta\theta} \\ \frac{1}{A_1A_2}\varepsilon^o_{s\theta} \\ \frac{1}{A_1}\gamma^o_{sz} \\ \frac{1}{A_2}\gamma^o_{s\theta} \end{Bmatrix} + z \begin{Bmatrix} \frac{1}{A_1}\kappa^o_{ss} \\ \frac{1}{A_2}\kappa^o_{\theta\theta} \\ \frac{1}{A_1A_2}\kappa^o_{s\theta} \\ 0 \\ 0 \end{Bmatrix} \right), \tag{9}$$

where

$$\frac{1}{A_1} = \frac{1}{1 + z/R_\phi} \quad \text{and} \quad \frac{1}{A_2} = \frac{1}{1 + z/R_\theta}.$$

R_ϕ and R_θ are the principle radii of curvature and z is the thickness variable of the shell along the z-coordinate. ε^o_{ss}, $\varepsilon^o_{\theta\theta}$, $\gamma^o_{s\theta}$ and κ^o_{ss}, $\kappa^o_{\theta\theta}$, $\kappa^o_{s\theta}$ are the mid-surface strains and curvatures. Following the definition of total *in-plane* force resultants ($N_{ss}, N_{\theta\theta}, N_{s\theta}$), resultant shear forces ($\bar{Q}_{ss}, \bar{Q}_{\theta\theta}$) and total moment resultants ($M_{ss}, M_{\theta\theta}, M_{s\theta}$), we have

$$\begin{Bmatrix} N_{ss} \\ N_{\theta\theta} \\ N_{s\theta} \end{Bmatrix} = \sum_{i\text{lay}=1}^{n\text{lay}} [Q]_{i\text{lay}} \left(\int_{h_{i\text{lay}-1}}^{h_{i\text{lay}}} \begin{Bmatrix} \frac{1}{A_1}\varepsilon^o_{ss} \\ \frac{1}{A_2}\varepsilon^o_{\theta\theta} \\ \frac{1}{A_1A_2}\gamma^o_{s\theta} \end{Bmatrix} \mathrm{d}z + z \begin{Bmatrix} \frac{1}{A_1}\kappa^o_{ss} \\ \frac{1}{A_2}\kappa^o_{\theta\theta} \\ \frac{1}{A_1A_2}\kappa^o_{s\theta} \end{Bmatrix} \mathrm{d}z \right), \tag{10}$$

$$\begin{Bmatrix} M_{ss} \\ M_{\theta\theta} \\ M_{s\theta} \end{Bmatrix} = \sum_{i\text{lay}=1}^{n\text{lay}} [Q]_{i\text{lay}} \left(\int_{h_{i\text{lay}-1}}^{h_{i\text{lay}}} z \begin{Bmatrix} \frac{1}{A_1}\varepsilon^o_{ss} \\ \frac{1}{A_2}\varepsilon^o_{\theta\theta} \\ \frac{1}{A_1A_2}\gamma^o_{s\theta} \end{Bmatrix} \mathrm{d}z + z^2 \begin{Bmatrix} \frac{1}{A_1}\kappa^o_{ss} \\ \frac{1}{A_2}\kappa^o_{\theta\theta} \\ \frac{1}{A_1A_2}\kappa^o_{s\theta} \end{Bmatrix} \mathrm{d}z \right). \tag{11}$$

Since the mid-surface strains ($\varepsilon^o_{ss}, \varepsilon^o_{\theta\theta}, \gamma^o_{s\theta}$) and curvatures ($\kappa^o_{ss}, \kappa^o_{\theta\theta}, \kappa^o_{s\theta}$) are independent of the z-axis, the integrals in Eqs. (10) and (11) become simple integrals of $(1, z, z^2)$. Thus, the loads and moments are related to the strains and curvature through the following relation.

$$\left\{ \begin{matrix} \mathbf{N} \\ \mathbf{M} \end{matrix} \right\} = \left[\begin{matrix} \bar{\mathbf{A}} & \bar{\mathbf{B}} \\ \bar{\bar{\mathbf{B}}} & \bar{\bar{\mathbf{D}}} \end{matrix} \right] \left\{ \begin{matrix} \boldsymbol{\varepsilon} \\ \boldsymbol{\kappa} \end{matrix} \right\} \tag{12}$$

In Eq. (12), the extensional terms $\bar{\mathbf{A}}$, bending–extensional coupling terms $\bar{\mathbf{B}}$ and bending terms $\bar{\mathbf{D}}$ are evaluated as follows

$$\bar{\mathbf{A}} = \sum_{i\text{lay}=1}^{n\text{lay}} Q_{ij}(z_{i\text{lay}+1} - z_{i\text{lay}}), \tag{13a}$$

$$\bar{\mathbf{B}} = \frac{1}{2} \sum_{i\text{lay}=1}^{n\text{lay}} Q_{ij}(z_{i\text{lay}+1}^2 - z_{i\text{lay}}^2). \tag{13b}$$

$$\bar{\mathbf{D}} = \frac{1}{3} \sum_{i\text{lay}=1}^{n\text{lay}} Q_{ij}(z_{i\text{lay}+1}^3 - z_{i\text{lay}}^3), \tag{13c}$$

where $i, j = 1, 2, 6$. The stress–strain relationship for shear in the $i$layth layer is expressed as

$$\begin{Bmatrix} \tau_{sz} \\ \tau_{\theta z} \end{Bmatrix}_{i\text{lay}} = \begin{bmatrix} Q_{44} & 0 \\ 0 & Q_{55} \end{bmatrix}_{i\text{lay}} \begin{Bmatrix} \gamma_{sz} \\ \gamma_{\theta z} \end{Bmatrix}_{i\text{lay}}. \tag{14}$$

The resultant shear forces $\bar{Q}_{ss}$ and $\bar{Q}_{\theta\theta}$ are defined as follows:

$$\begin{Bmatrix} \bar{Q}_{ss} \\ \bar{Q}_{\theta\theta} \end{Bmatrix} = \sum_{i\text{lay}=1}^{n\text{lay}} \int_{h_{i\text{lay}-1}}^{h_{i\text{lay}}} \begin{bmatrix} Q_{44} & 0 \\ 0 & Q_{55} \end{bmatrix}_{i\text{lay}} \begin{Bmatrix} \frac{1}{A_1}\gamma_{sz} \\ \frac{1}{A_2}\gamma_{\theta z} \end{Bmatrix}_{i\text{lay}} \mathrm{d}z. \tag{15}$$

A shear correction factor of 5/6 is used during the evaluation of A_{44} and A_{55}:

$$\begin{Bmatrix} \bar{Q}_{ss} \\ \bar{Q}_{\theta\theta} \end{Bmatrix} = \begin{bmatrix} \bar{A}_{44} & 0 \\ 0 & \bar{A}_{55} \end{bmatrix}_{i\text{lay}} \begin{Bmatrix} \gamma_{sz} \\ \gamma_{\theta z} \end{Bmatrix}_{i\text{lay}}, \tag{16}$$

where

$$\bar{A}_{ij} = \frac{5}{6} \sum_{i\text{lay}=1}^{n\text{lay}} Q_{ij} \int_{h_{i\text{lay}-1}}^{h_{i\text{lay}}} 1 \, \mathrm{d}z. \tag{17}$$

This completes the detailed description on the evaluation of the constitutive matrix for a functionally graded cylindrical shell. The stiffness matrix is obtained from the strain energy and the element stiffness matrix corresponding to the mth harmonic is computed as follows

$$\mathbf{k}_e = \int_A \mathbf{B}^{*\mathrm{T}} \bar{\bar{\mathbf{D}}} \mathbf{B}^* r \, \mathrm{d}s \, \mathrm{d}\theta, \tag{18}$$

where $\mathbf{B}^*$ is the strain–displacement matrix, $\bar{\bar{\mathbf{D}}}$ is the reduced stiffness coefficient obtained based on the description following Eqs. (13a–c) and (17) and r represents the mid-surface radius of shell. The element stiffness matrix is assembled using the standard assembly procedure in finite element analysis to obtain the global stiffness matrix, $\mathbf{K}^{uu} = \sum \mathbf{k}_e$. The mass matrix is obtained from the

kinetic energy:

$$\mathrm{KE} = \frac{\rho}{2}\int_V (\dot{u}^2 + \dot{v}^2 + \dot{w}^2)\,\mathrm{d}V = \frac{\rho}{2}\int_V \mathbf{u}^{\mathrm{T}}\mathbf{u}\,\mathrm{d}V = \frac{1}{2}\,\mathbf{d}^{\mathrm{T}}\mathbf{m}_e\mathbf{d}, \tag{19}$$

where $\mathbf{u} = \bar{\mathbf{N}}\mathbf{d}$. $\bar{\mathbf{N}}$ is the shape function matrix for a three-node quadratic line element expressed in terms of the isoparametric coordinate, β, as follows:

$$\bar{N}_1 = \frac{(\beta^2 - \beta)}{2}, \quad \bar{N}_2 = (1 - \beta^2) \quad \text{and} \quad \bar{N}_3 = \frac{(\beta^2 + \beta)}{2}$$

in which $\beta = -1, 0$ and $+1$ at node 1, 2 and 3. $\mathbf{d}$ is a vector of nodal displacement,

$$\mathbf{d}^{\mathrm{T}} = \{u_{o1}, v_{o1}, w_{o1}, \psi_{os1}, \psi_{o\theta 1}, u_{o2}, v_{o2}, w_{o2}, \psi_{os2}, \psi_{o\theta 2}, u_{o3}, v_{o3}, w_{o3}, \psi_{os3}, \psi_{o\theta 3}\},$$

where u_o, v_o, and w_o are displacements of the mid-surface along the s, θ and z directions and ψ_{os} and $\psi_{o\theta}$ are the bending rotations of the normal to the mid-surface along s and θ directions, respectively. Suffixes 1, 2 and 3 denote the node number. $\mathbf{m}_e$ is the element mass matrix given by

$$\mathbf{m}_e = \bar{\rho}_{\mathrm{eff}}\int_A \bar{\mathbf{N}}^{\mathrm{T}}\bar{\mathbf{N}}\,\mathrm{d}A, \tag{20}$$

where

$$\bar{\rho}_{\mathrm{eff}} = \sum_{i\mathrm{lay}=1}^{n\mathrm{lay}} \int_{h_{i\mathrm{lay}}}^{h_{i\mathrm{lay}+1}} \rho_{\mathrm{eff}}\,\mathrm{d}z.$$

The computation of the mass matrix involves the use of effective density of the FGM shell as described in Eq. (4c).

Linear thermal buckling analysis of FGM cylindrical shell is required to be framed. A discussion on the classical initial stability problems may be found in Zienkiewicz and Taylor [31]. The initial stiffness matrix (or geometric stiffness matrix) due to thermal loading is evaluated as follows:

$$\mathbf{k}_{\sigma e} = \int_A \mathbf{B}^{i\mathrm{T}}\mathbf{N}^{*\mathrm{th}}\mathbf{B}^{i}\,\mathrm{d}A, \tag{21}$$

where $\mathbf{B}^i$ is the strain–displacement matrix based on strains due to large deformation, Ross [32], and $\mathbf{N}^{*\mathrm{th}}$ is a matrix of initial stress resultants due to temperature rise. Assembling the element geometric stiffness matrix yields the global geometric stiffness matrix, $\mathbf{K}_{\sigma}^{uu} = \sum \mathbf{k}_{\sigma e}$. The thermal stresses in the $i$layth layer of the FGM shell are

$$\left\{\begin{array}{c}\sigma_{ss}\\ \sigma_{\theta\theta}\\ \sigma_{s\theta}\end{array}\right\}^{\mathrm{th}}_{i\mathrm{lay}} = [Q]_{i\mathrm{lay}}\left\{\begin{array}{c}\alpha_{ss}\\ \alpha_{\theta\theta}\\ 0\end{array}\right\}\Delta T. \tag{22}$$

The thermal loads and moments are defined as follows:

$$\mathbf{N}^{\mathrm{th}} = \begin{Bmatrix} N_{ss}^{\mathrm{th}} \\ N_{\theta\theta}^{\mathrm{th}} \\ N_{s\theta}^{\mathrm{th}} \end{Bmatrix} = \int_{-h/2}^{h/2} \begin{Bmatrix} \sigma_{ss} \\ \sigma_{\theta\theta} \\ \tau_{s\theta} \end{Bmatrix}_{i\mathrm{lay}}^{\mathrm{th}} \mathrm{d}z = \sum_{i\mathrm{lay}=1}^{n\mathrm{lay}} [Q]_{i\mathrm{lay}} \begin{Bmatrix} \alpha_{ss} \\ \alpha_{\theta\theta} \\ 0 \end{Bmatrix}_{i\mathrm{lay}} \Delta\mathrm{Th}, \tag{23a}$$

$$\mathbf{M}^{\mathrm{th}} = \begin{Bmatrix} M_{ss}^{\mathrm{th}} \\ M_{\theta\theta}^{\mathrm{th}} \\ M_{s\theta}^{\mathrm{th}} \end{Bmatrix} = \int_{-h/2}^{h/2} z \begin{Bmatrix} \sigma_{ss} \\ \sigma_{\theta\theta} \\ \tau_{s\theta} \end{Bmatrix}_{i\mathrm{lay}}^{\mathrm{th}} \mathrm{d}z = \sum_{i\mathrm{lay}=1}^{n\mathrm{lay}} [Q]_{i\mathrm{lay}} \begin{Bmatrix} \alpha_{ss} \\ \alpha_{\theta\theta} \\ 0 \end{Bmatrix} \Delta\mathrm{T}(h_{i\mathrm{lay}} - h_{i\mathrm{lay}-1}) \frac{(h_{i\mathrm{lay}} + h_{i\mathrm{lay}-1})}{2}. \tag{23b}$$

In the above Eqs. (23a) and (23b), the coefficient of thermal expansion $\alpha_{ss} = \alpha_{\theta\theta}$. α_{ss} and $\alpha_{\theta\theta}$ are obtained using Eq. (4e). After computing the thermal load, the total stress resultants and moment resultants are determined (Ref. [33]) as follows

$$\bar{\mathbf{N}}^{\mathrm{th}} = \bar{\bar{\mathbf{D}}}\boldsymbol{\varepsilon}_o - \begin{Bmatrix} \mathbf{N}^{\mathrm{th}} \\ \mathbf{M}^{\mathrm{th}} \end{Bmatrix}, \tag{24}$$

where $\boldsymbol{\varepsilon}_o$ is the strain vector due to mechanical deflection arising from thermal loading. The initial stress resultants and moment resultants vector, $\bar{\mathbf{N}}^{\mathrm{th}}$, will be used to compose the initial stress resultants matrix $\mathbf{N}^{*\mathrm{th}}$ as follows and will be used in Eq. (21):

$$\begin{bmatrix} \bar{N}_{ss}^{\mathrm{th}} & \bar{N}_{s\theta}^{\mathrm{th}} & \bar{M}_{ss}^{\mathrm{th}} & \bar{M}_{s\theta}^{\mathrm{th}} \\ \bar{N}_{s\theta}^{\mathrm{th}} & \bar{N}_{\theta\theta}^{\mathrm{th}} & \bar{M}_{s\theta}^{\mathrm{th}} & \bar{M}_{\theta\theta}^{\mathrm{th}} \\ \bar{M}_{ss}^{\mathrm{th}} & \bar{M}_{s\theta}^{\mathrm{th}} & \bar{Q}_{ss}^{\mathrm{th}} & \bar{Q}_{s\theta}^{\mathrm{th}} \\ \bar{M}_{s\theta}^{\mathrm{th}} & \bar{M}_{\theta\theta}^{\mathrm{th}} & \bar{Q}_{s\theta}^{\mathrm{th}} & \bar{Q}_{\theta\theta}^{\mathrm{th}} \end{bmatrix}.$$

2.3. 1D heat conduction analysis for FGM cylindrical shells

A steady-state 1D heat conduction analysis is considered to evaluate the temperature distribution across the thickness of the FGM shell based on the temperature specified boundary condition. Fig. 1 describes the problem considered for the steady-state heat conduction analysis.

The finite element equation for this situation is as follows: $\mathbf{K}_{\mathrm{con}}\hat{\mathbf{T}} = 0$, where $\mathbf{K}_{\mathrm{con}}$ is the heat conduction matrix and $\hat{\mathbf{T}}$ is a vector of nodal temperature (Ref. [34]). Subsequent to this, the structural analysis is carried out.

The computer code has been extended to compute the temperature distribution across the wall of the FGM shell by taking into account the material properties as a function of temperature. An iterative procedure is followed in order to obtain a converged temperature distribution in the

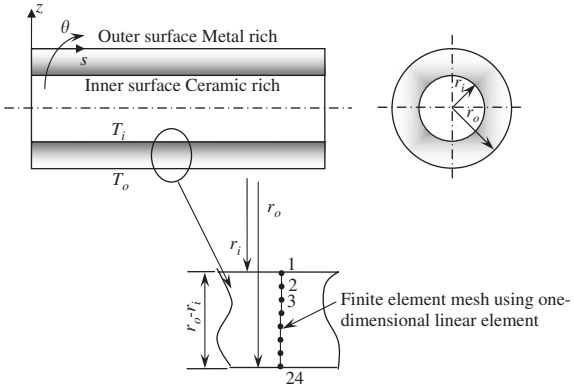

Fig. 1. Schematic illustration of the steady-state heat conduction through the wall of a hollow cylinder.

subsequent studies. The description of the procedure is well understood through the flow chart (Fig. 2).

3. Results and discussions

3.1. Linear thermal buckling analysis of functionally graded cylindrical shells

The evaluation of critical buckling temperature (or bifurcation buckling temperature) is based on the classical stability equation involving the structural stiffness matrix, $\mathbf{K}^{uu}$, and initial stiffness matrix, $\mathbf{K}_{\sigma}^{uu}$. The buckling eigenvalues and buckling mode shapes are computed using the simultaneous iteration technique. A typical configuration of the functionally graded cylindrical shell is assumed to be ceramic rich on the inner surface and metal rich on the outer surface. Following are the functionally graded cylindrical shells considered for study

(i) functionally graded cylindrical shell composed of SUS304/Si_3N_4,
(ii) functionally graded cylindrical shell composed of SUS304/Al_2O_3,
(iii) functionally graded cylindrical shell composed of SUS304/ZrO_2,
(iv) functionally graded cylindrical shell composed of Ti–6Al–4V/Si_3N_4,
(v) functionally graded cylindrical shell composed of Ti–6Al–4V/Al_2O_3,
(vi) functionally graded cylindrical shell composed of Ti–6Al–4V/ZrO_2.

The material properties are taken from the literature of Reddy and Chin [4]. The geometric details of the FGM cylindrical shell are listed in Table 1. The numerical studies are limited to the clamped–clamped boundary condition.

A rigorous analysis to compute the bifurcation buckling temperature for functionally graded cylindrical shells based on uncoupled thermomechanical formulation follows. The analysis considers a case of FGM cylindrical shell with temperature varying across the wall thickness. The temperature gradient along the length of the shell is negligible. Given the temperature boundary

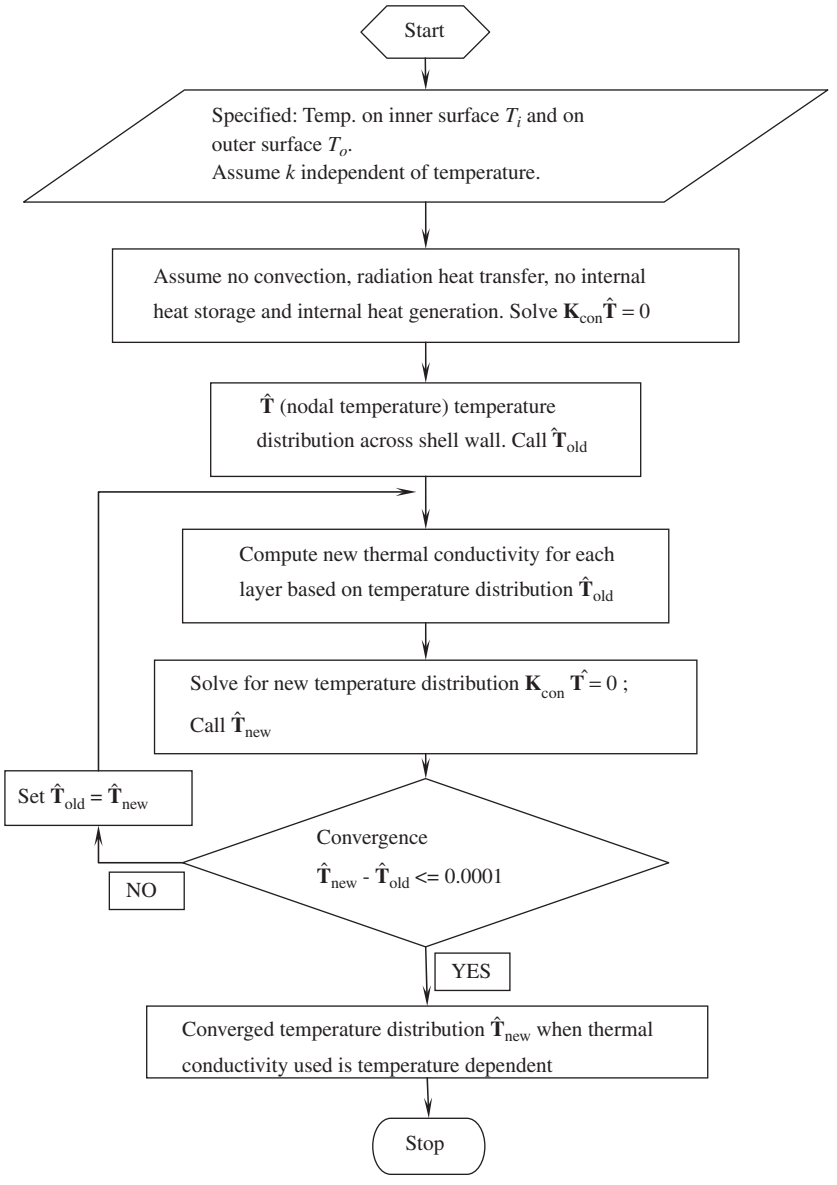

Fig. 2. Flow chart for computation of temperature distribution across the thickness of the shell based on temperature-dependent material properties.

conditions, i.e. temperature specified on the inner and the outer surfaces of the cylindrical shell, a simple steady-state heat conduction analysis yields the temperature distribution across the shell wall. The temperature distribution evaluated is based on the temperature-dependent material property (i.e. thermal conductivity). Thus, it is required to iterate until a converged temperature distribution is obtained. This temperature distribution now represents the thermal loading on the

Table 1
Geometry details of FGM cylindrical shells

Sl. no.	Radius, r (m)	Length, l (m)	Thickness, h (m)	l/r	r/h
1	0.876	0.9144	0.00876	1.0438	100
2	0.876	4.572	0.00438	5.219	200

FGM shell, which results in thermal stresses. Based on converged temperature distribution the mechanical properties and thermal property are evaluated. Initial stresses are computed to carry out the bifurcation thermal buckling analysis. The thermal buckling temperature thus obtained will be based on not only the converged temperature distribution across the wall thickness but also on the converged thermal stresses, which means to say that the arbitrary high temperature specified on the shell wall will change until a converged buckling temperature is obtained. Thus, a two-stage iterative procedure is adopted, which brings about convergence of not only the temperature distribution but also the thermal stresses. The total effective stresses due to thermal loading are used to evaluate the geometric stiffness matrix. Thus, linear thermal buckling analysis is carried out to obtain the buckling eigenvalues and buckling eigenvectors. The overall procedure followed for the determination of the thermal buckling temperature is best understood from the flow chart presented in Fig. 3. The error between the critical buckling temperature obtained between the previous step and the new step is chosen to be less than or equal to 0.5. The loop for checking the convergence of the buckling temperature is initiated by setting a large error. The first critical buckling temperature obtained is set as the old buckling temperature. This temperature is now set as specified temperature on the inner surface of the cylinder and the outer surface of the cylindrical shell is always set at ambient temperature 27 °C. This leads to the computation of the new buckling temperature, which starts from the step involving the determination of temperature distribution across the shell wall and so on (Fig. 3). Now a real check on the buckling temperature is made between the old buckling temperature and the new buckling temperature, which yields an error. This error should be less than or equal to 0.5 to obtain the converged buckling temperature.

3.2. Convergence studies

A convergence study is taken up in order to determine a suitable number of homogeneous layers as well as the number of finite elements required for the evaluation of the constitutive matrix and hence the buckling temperature. Independent convergence studies are required depending on the length-to-radius ratio of the shells (Table 1). The convergence study involves determining the buckling temperature based on the iterative procedure discussed previously. Consider the convergence study for an FGM cylindrical shell with length-to-radius ratio $(l/r) = 5.21$, radius-to-thickness ratio $(r/h) = 200$ and mean radius r equal to 0.876 meter. The FGM shell is composed of SUS304/Si_3N_4. The number of finite elements for the cylindrical shell geometry varied from 30 elements to 80 elements. For each of the finite element mesh, the thickness of the shell was divided into (i) five layers, (ii) ten layers, (ii) 20 layers and (iii) 40 layers. Thermal buckling temperatures were evaluated for the four models for various values of the

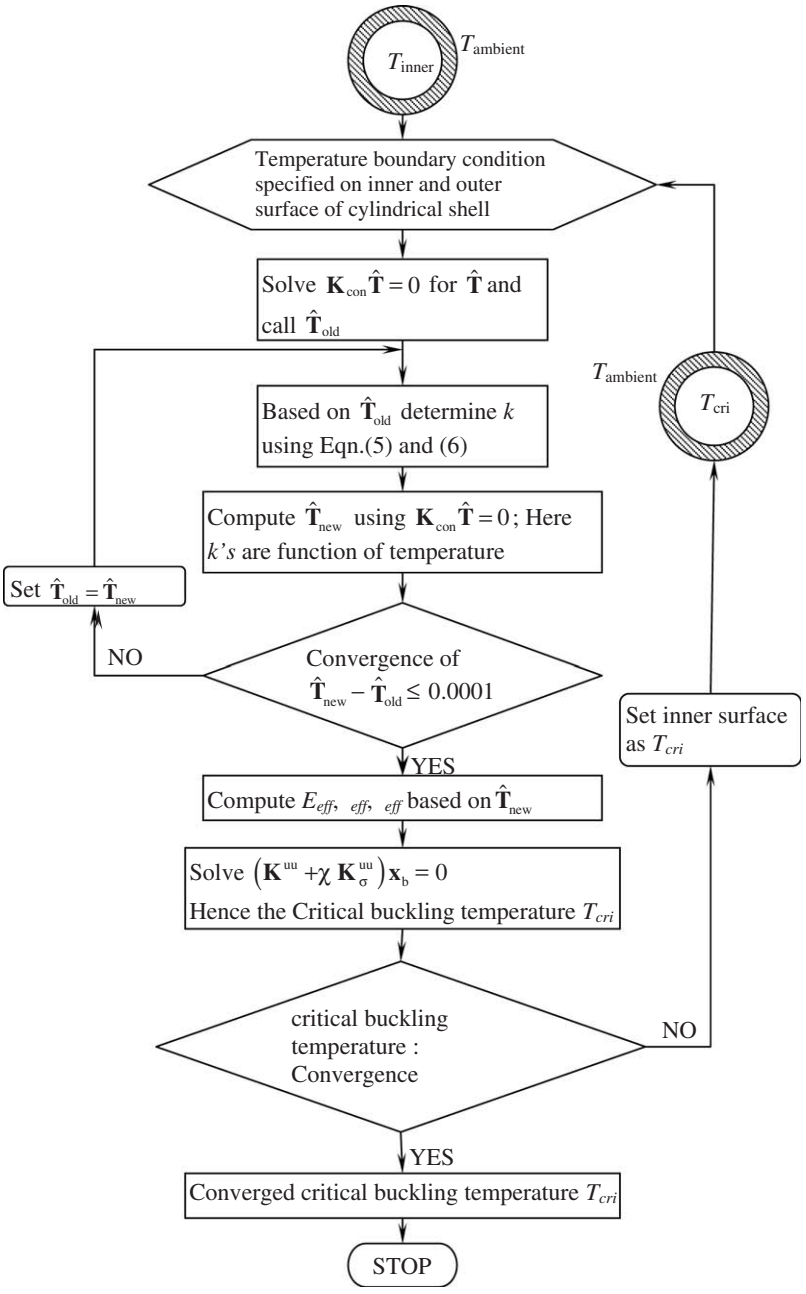

Fig. 3. Flow chart describing the overall evaluation procedure to obtain converged lowest thermal buckling temperature.

power-law index. It was found that for a given finite element mesh, the buckling temperature converged for FGM shell with 20 and 40 layers. Typical convergence results are presented in Table 2 for a finite element mesh having 60 elements. The percentage difference in the buckling temperature predicted by the 20-layered model and the 40-layered model is less when compared to the 10-layered model and the 20-layered model. With this observation it is reasonable to use the 20-layered model to represent the shell thickness for the evaluation of the mechanical and thermal properties. As far as the number of finite elements was concerned, the buckling temperature converged for the finite element mesh beyond 70 (refer to Table 3). Similar studies for the FGM cylindrical shell with $l/r = 1.0438$ were carried out and it was found that a finite element mesh with 30 elements and 20 layers was sufficient.

Table 2
Convergence study for the choice of number of layers for FGM shell thickness FE model with 60 elements

Power-law index $\underline{n}$	Critical thermal buckling temperature T_{cri} (°C) for			
	5 layers	10 layers	20 layers	40 layers
0.0 (metal rich)	358.86	358.45	358.21	358.22
0.05	371.47	371.85	372.23	372.39
0.10	383.85	385.39	386.21	386.62
0.50	480.81	487.26	489.76	490.84
1.00	573.04	577.83	579.15	579.50
5.00	692.17	691.13	690.82	690.74
10.0	694.38	693.31	692.60	692.33
15.0	693.39	692.70	692.00	691.72
100.0	689.63	689.91	690.40	690.43
$\gg 100.0$ (ceramic rich)	689.57	690.03	690.04	690.14

Table 3
Convergence study for the choice of number of finite elements for FGM shell with $l/r = 5.21$

Power-law index $\underline{n}$	Critical thermal buckling temperature T_{cri} (°C) for			
	50 elements	60 elements	70 elements	80 elements
0.0 (metal rich)	357.54	358.21	358.18	358.05
0.05	371.55	372.23	372.16	372.00
0.10	385.56	386.21	386.18	386.02
0.50	488.95	489.76	489.70	489.54
1.00	578.03	579.15	579.04	578.88
5.00	689.29	690.82	690.77	690.56
10.0	691.14	692.60	692.50	692.24
15.0	690.58	692.00	691.90	691.62
100.0	689.31	690.40	690.36	690.00
$\gg 100.0$ (ceramic rich)	688.97	690.04	689.91	689.56

FGM shell is assumed to be 20 layers thick.

Table 4
Comparison of thermal buckling temperature of composite shells as obtained using the formulation for FGM shells

r/h	Critical buckling temperature, ΔT_{cri} (°C)	
	Semi-loof finite element method, Thangaratnam et al. (1989)	Results from the present study
200	1304.298 (11,1)	1258.4 (11,1)
300	912.434 (13,1)	851.3 (13,1)
400	659.610 (18,1)	637.8 (18,1)
500	514.745 (19,1)	507 (19,1)

3.3. Validation of the thermal buckling temperature of cylindrical shells

The semianalytical finite element formulation for the analysis of thermal buckling temperature for FGM shells of revolution has been validated by evaluating the critical buckling temperature of composite cylindrical shells as reported by Thangaratnam et al. [35]. Using semiloof finite element, Thangaratnam et al. carried out finite element analysis of buckling of composite cylindrical shells under the influence of mechanical and thermal loads. Table 4 lists the comparison of results on buckling temperature of the composite cylindrical shell under uniform temperature rise with a simply supported boundary condition. This is resorted to primarily because of the lack of literature on the evaluation of buckling temperature of FGM shells using the finite element method.

3.4. Validation of transient thermal response for functionally graded hollow cylinder conveying hot gases

Praveen et al. [36] carried out transient response studies on a functionally graded hollow cylinder conveying hot gases. A transient study is presented demonstrating the temperature rise and temperature distribution across the wall of the cylinder with the passage of time resulting from the high-temperature gases rushing into the cylinder. The results reported consider material properties dependent on temperature. The boundary conditions are (i) the outer surface of the hollow cylinder is well insulated and (ii) the inner surface is subjected to a convection condition due to flow of hot gases, Fig. 4 (a). With the objective to reproduce the temperature distribution across the cylinder wall due to the flow of hot gases into the functionally graded hollow cylinder as a function of time, an axisymmetric heat transfer finite element is formulated. The formulation is based on the functional for heat transfer problem as discussed by Rao [37], and the functional is simplified to the current problem definition. The finite element form of the unsteady state heat transfer problem for the boundary conditions as stated in the beginning is represented by the following equation:

$$\mathbf{K}_{\text{cap}}\dot{\hat{\mathbf{T}}} + (\mathbf{K}_{\text{cond}} + \mathbf{K}_{\text{conv}})\hat{\mathbf{T}} = \mathbf{P}_{\text{H}}. \tag{25}$$

In Eq. (25) $\mathbf{K}_{\text{cond}}$ and $\mathbf{K}_{\text{conv}}$ represent the heat conduction and convective matrices of the system, respectively. The matrix $\mathbf{K}_{\text{cap}}$ arises due to a change in the internal energy of the system and this

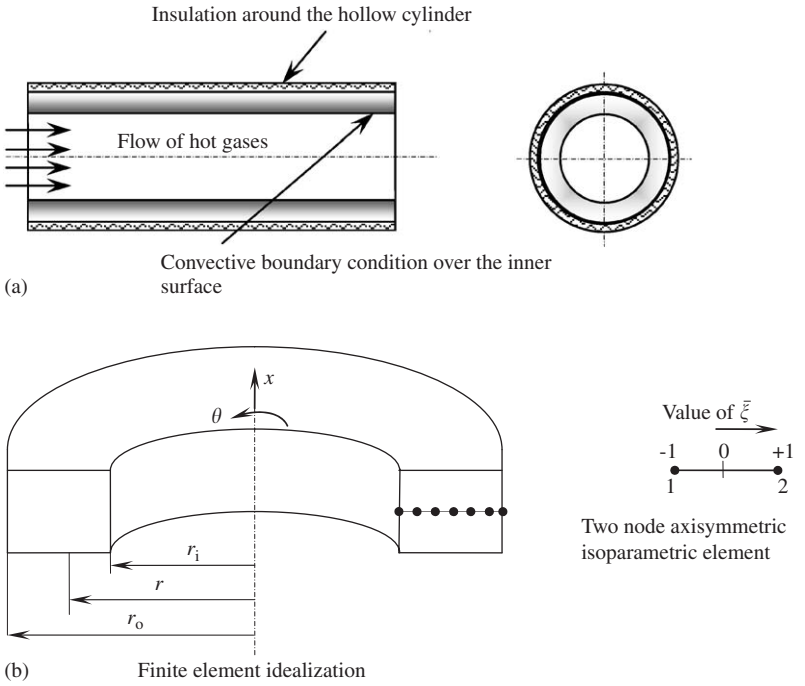

Fig. 4. Flow of hot gases through a functionally graded hollow cylinder and the associated boundary conditions (a) and finite element idealization using a two-node isoparametric element in the radial direction for the analysis (b).

term in Eq. (25) governs the transient behavior of the system. These equations must be solved for the variation of $\hat{\mathbf{T}}$ in space and time; $\hat{\mathbf{T}} = \{\hat{T}_1 \hat{T}_2 \hat{T}_3 \hat{T}_4 \ldots \hat{T}_{n\text{odt}}\}^{\mathrm{T}}$ is the vector of nodal temperature for the system.

A methodology discussed based on finite difference approximation in the time domain is applied to generate a numerical solution for Eq. (25) may be found in Segerlind [38]. The material properties are evaluated at the stated temperature during the transient response evaluation. Data for the problem: The functionally graded hollow cylinder is composed of Zirconia and Titanuim alloy (Ti6AlV). The material properties are listed in Praveen et al. [36]. The hollow cylinder has the following dimensions: inner radius = 0.0127 m and outer radius = 0.0254 m. Initially, the hollow cylinder is at room temperature of 25.15 °C. The temperature of the hot gases flowing within the hollow cylinder was assumed to be 1827 °C and the heat transfer coefficient was assumed to be 750 $\mathrm{W/m^2K}$. The time step chosen was 5.0×10^{-5} s. Numerical computation was undertaken to produce results on the temperature distribution across the wall of the hollow cylinder for time periods of 0.2, 0.4, 0.6, 0.8 and 1.0 s. The material properties were updated based on the temperature distribution obtained at the end of the each iteration. Initial rise in temperature on the inner surface of the shell wall for various time intervals as obtained by Praveen et al. and from the present procedure is listed in Table 5. It is observed that the results tally well with a small percentage difference.

Table 5
Comparison of initial temperature rise on the inner surface of FGM shell wall

Time in seconds	Initial temperature rise °C on the inner shell wall		% difference
	Praveen et al. [36]	Present	
0.2	260	240	7.6
0.4	340	310	8.8
0.6	390	355	8.9
0.8	425	400	5.8
1.0	455	430	5.5

Table 6
Comparison of critical buckling temperature without iteration Case (a) and with iteration Case (b). FGM cylindrical shell: $l/r = 1.0438$, $r/h = 200$, Ti–6Al–4V/ZrO_2

Power-law index	Case (a)	Case (b)
0.0 (metal rich)	539.37 (13,1)	355.75 (13,1)
0.05	520.16 (13,1)	337.65 (13,1)
0.1	504.29 (13,1)	324.84 (13,1)
0.5	444.84 (13,1)	292.73 (13,1)
1.0	421.38 (13,1)	292.79 (13,1)
5.0	364.23 (13,1)	256.89 (13,1)
10.0	349.22 (13,1)	242.76 (13,1)
15.0	343.85 (13,1)	237.58 (13,1)
100.0	334.89 (13,1)	228.27 (13,1)
$\geqslant$100.00 (ceramic rich)	333.01 (13,1)	226.56 (13,1)

Thus, the foregoing validations have strengthened the computational aspects that are essential for the present work on the computation of thermal buckling behavior of functionally graded cylindrical shells which consider temperature-dependent material properties.

3.5. Case study to illustrate the significance of considering temperature-dependent material properties in FGM

An exercise is taken up to illustrate the necessity of considering temperature-dependent material properties. For the sake of illustration two exercises are executed:

Case (a) critical (or bifurcation) buckling temperature for FGM shell is obtained by computing the temperature distribution across the thickness of the shell with specified arbitrary high temperature on the inner surface and ambient temperature on the outer surface. The temperature distribution obtained is based on the thermal properties assumed at room temperature. The temperature distribution thus obtained becomes the thermal load on the shell. Thermal buckling temperature is computed and the material properties used are as per room temperature. Case (b) critical buckling temperatures are computed based on the procedure illustrated in Fig. 3. The results are presented in Table 6 for FGM shell viz., Ti–6Al–4V–ZrO_2. The buckling temperature

estimated according to the procedure of Case (a) is higher when compared to the buckling temperature computed using the procedure of Case (b).

3.6. Critical thermal buckling temperature of FGM shells—parametric study

Following the procedure outlined in the flow chart, Fig. 3, computation of thermal buckling temperature for FGM cylindrical shells is taken up. Shells with two ratios of r/h are considered and for each r/h ratio, two l/r ratios are considered for the study. The power-law indexes for the study are chosen as $\underline{n} = 0.0, 0.05, 0.1, 0.5, 1.0, 5.0, 10.0, 15.0, 100.0, \gg 100.0$. The lowest or critical buckling temperature and the associated mode number are listed in Tables 7–12, for a combination of metal and ceramic FGMs. For values of $\underline{n} = 0.0$, the FGM cylindrical shell

Table 7
Critical buckling temperature T_{cri} in °C for FGM of SUS304 and Si_3N_4

Power-law index $\underline{n}$	$r/h = 100$		$r/h = 200$	
	$l/r = 1.0438$	$l/r = 5.21$	$l/r = 1.0438$	$l/r = 5.21$
0.0 (metal rich)	598.98 (9,1)	625.12 (9,1)	346.33 (13,1)	358.18 (13,1)
0.05	622.28 (9,1)	648.97 (9,1)	359.98 (13,1)	372.16 (13,1)
0.1	645.81 (9,1)	673.20 (9,1)	373.55 (13,1)	386.18 (13,1)
0.5	826.33 (9,1)	858.90 (9,1)	474.58 (13,1)	489.70 (13,1)
1.0	984.05 (9,1)	1019.52 (9,1)	561.94 (13,1)	579.04 (13,1)
5.0	1151.96 (9,1)	1184.82 (9,1)	673.24 (13,1)	690.77 (13,1)
10.0	1147.37 (9,1)	1178.57 (9,1)	675.50 (13,1)	692.50 (13,1)
15.0	1144.26 (9,1)	1175.03 (9,1)	675.02 (13,1)	691.90 (13,1)
100.0	1139.17 (9,1)	1168.76 (9,1)	673.78 (13,1)	690.36 (13,1)
$\gg 100.00$ (ceramic rich)	1138.35 (9,1)	1168.30 (9,1)	673.40 (13,1)	689.91 (13,1)

Table 8
Critical buckling temperature T_{cri} in °C for FGM shell of SUS304 and aluminum oxide

Power-law index $\underline{n}$	$r/h = 100$		$r/h = 200$	
	$l/r = 1.0438$	$l/r = 5.21$	$l/r = 1.0438$	$l/r = 5.21$
0.0 (metal rich)	598.98 (9,1)	625.12 (9,1)	346.33 (13,1)	358.18 (13,1)
0.05	581.98 (9,1)	607.40 (9,1)	336.91 (13,1)	348.39 (13,1)
0.1	579.91 (9,1)	604.76 (9,1)	335.57 (13,1)	346.91 (13,1)
0.5	637.58 (9,1)	663.77 (9,1)	367.05 (13,1)	378.79 (13,1)
1.0	714.62 (9,1)	742.39 (9,1)	409.70 (13,1)	422.23 (13,1)
5.0	994.02 (9,1)	1027.84 (9,1)	564.61 (13,1)	580.52 (13,1)
10.0	1106.30 (9,1)	1143.62 (9,1)	626.97 (13,1)	644.44 (13,1)
15.0	1158.08 (9,1)	1196.85 (9,1)	655.77 (13,1)	673.99 (13,1)
100.0	1265.14 (9,1)	1307.57 (9,1)	715.91 (13,1)	735.68 (13,1)
$\gg 100.00$ (ceramic rich)	1271.07 (9,1)	1313.59 (9,1)	719.16 (13,1)	739.10 (13,1)

Table 9
Critical buckling temperature T_{cri} in °C for FGM shell of SUS304 and zirconia

Power-law index $\underline{n}$	$r/h = 100$		$r/h = 200$	
	$l/r = 1.0438$	$l/r = 5.21$	$l/r = 1.0438$	$l/r = 5.21$
0.0 (metal rich)	598.98 (9,1)	625.12 (9,1)	346.33 (13,1)	358.18 (13,1)
0.05	545.67 (9,1)	565.39 (9,1)	330.48 (13,1)	340.92 (13,1)
0.1	516.24 (9,1)	534.26 (9,1)	321.04 (13,1)	330.84 (13,1)
0.5	478.91 (9,1)	492.69 (9,1)	314.80 (13,1)	323.03 (13,1)
1.0	497.44 (9,1)	511.09 (9,1)	330.96 (13,1)	339.15 (13,1)
5.0	425.00 (9,1)	436.73 (9,1)	284.25 (13,1)	291.48 (13,1)
10.0	390.15 (9,1)	400.56 (9,1)	259.28 (13,1)	265.80 (13,1)
15.0	375.68 (9,1)	386.42 (9,1)	249.46 (13,1)	255.64 (13,1)
100.0	347.61 (9,1)	357.30 (9,1)	229.31 (13,1)	235.01 (13,1)
$\gg 100.00$ (ceramic rich)	343.30 (9,1)	353.31 (9,1)	226.54 (13,1)	232.19 (13,1)

Table 10
Critical buckling temperature T_{cri} in °C for FGM shell of Ti–6Al–4V and Si_3N_4

Power-law index $\underline{n}$	$r/h = 100$		$r/h = 200$	
	$l/r = 1.0438$	$l/r = 5.21$	$l/r = 1.0438$	$l/r = 5.21$
0.0 (metal rich)	540.69 (9,1)	556.33 (9,1)	354.47 (13,1)	363.48 (13,1)
0.05	547.85 (9,1)	563.67 (9,1)	359.10 (13,1)	368.05 (13,1)
0.1	557.66 (9,1)	574.00 (9,1)	365.09 (13,1)	374.08 (13,1)
0.5	676.69 (9,1)	695.28 (9,1)	428.65 (13,1)	439.31 (13,1)
1.0	815.61 (9,1)	838.40 (9,1)	496.18 (13,1)	508.55 (13,1)
5.0	1067.12 (9,1)	1096.46 (9,1)	620.67 (13,1)	636.08 (13,1)
10.0	1095.24 (9,1)	1124.30 (9,1)	641.29 (13,1)	656.98 (13,1)
15.0	1106.34 (9,1)	1135.81 (9,1)	650.10 (13,1)	665.97 (13,1)
100.0	1136.17 (9,1)	1166.14 (9,1)	671.88 (13,1)	688.48 (13,1)
$\gg 100.00$ (ceramic rich)	1138.35 (9,1)	1168.19 (9,1)	673.40 (13,1)	689.91 (13,1)

corresponds to an isotropic shell with properties corresponding to that of metal and $\underline{n} \gg 100.0$ corresponds to a cylindrical shell purely of ceramic material. The power-law indexes other than the two extreme values govern the distribution profiles of metal in the FGM shell.

The critical buckling temperatures for FGM shells made from a combination of SUS304 and three ceramics are considered here. Certain important observations apparent from Tables 7–9 are as follows: (i) For SUS304/Si_3N_4 FGM shells the critical thermal buckling temperatures are high and decrease marginally for $\underline{n}$ ranging between 5.0 and 100.0 and for large values of the power-law index (i.e. rich in ceramics). For $\underline{n}$ ranging from 0.0 to 5.0 the critical buckling temperatures increase as $\underline{n}$ increases. (ii) For SUS304–Al_2O_3 FGM shells the critical buckling temperatures are high for ceramic composition, i.e. $\underline{n} = 100$ and $\underline{n} \gg 100.0$. The critical buckling temperatures decrease as the power-law index increases from $\underline{n} = 0.0$ to 0.1, and for $\underline{n} > 0.5$ the buckling temperatures increase with increase in the power-law index.

Table 11
Critical buckling temperature in °C for FGM shell of Ti–6Al–4V and aluminum oxide

Power-law index $\underline{n}$	$r/h = 100$		$r/h = 200$	
	$l/r = 1.0438$	$l/r = 5.21$	$l/r = 1.0438$	$l/r = 5.21$
0.0 (metal rich)	541.00 (9,1)	551.15 (9,1)	354.64 (13,1)	360.34 (13,1)
0.05	518.75 (9,1)	528.54 (9,1)	339.49 (13,1)	345.17 (13,1)
0.1	511.67 (9,1)	520.98 (9,1)	333.80 (13,1)	339.45 (13,1)
0.5	544.18 (9,1)	553.86 (9,1)	347.92 (13,1)	353.55 (13,1)
1.0	609.47 (9,1)	620.20 (9,1)	381.46 (13,1)	387.47 (13,1)
5.0	917.80 (9,1)	935.44 (9,1)	532.47 (13,1)	541.42 (13,1)
10.0	1058.46 (9,1)	1080.29 (9,1)	602.43 (13,1)	612.92 (13,1)
15.0	1122.87 (9,1)	1146.28 (9,1)	636.34 (13,1)	647.54 (13,1)
100.0	1262.21 (9,1)	1289.67 (9,1)	714.33 (13,1)	727.28 (13,1)
$\gg 100.00$ (ceramic rich)	1271.07 (9,1)	1298.46 (9,1)	719.16 (13,1)	732.28 (13,1)

Table 12
Critical buckling temperature T_{cri} in °C for FGM shell of Ti–6Al–4V and zirconia

Power-law index $\underline{n}$	$r/h = 100$		$r/h = 200$	
	$l/r = 1.0438$	$l/r = 5.21$	$l/r = 1.0438$	$l/r = 5.21$
0.0 (metal rich)	542.29 (9,1)	558.23 (9,1)	355.75 (13,1)	364.49 (13,1)
0.05	510.29 (9,1)	524.71 (9,1)	337.65 (13,1)	346.08 (131)
0.1	487.82 (9,1)	501.36 (9,1)	324.84 (13,1)	332.61 (13,1)
0.5	436.08 (9,1)	447.77 (9,1)	292.73 (13,1)	299.75 (13,1)
1.0	439.09 (9,1)	451.32 (9,1)	292.79 (13,1)	299.97 (13,1)
5.0	387.90 (9,1)	398.75 (9,1)	256.89 (13,1)	263.10 (13,1)
10.0	367.42 (9,1)	377.20 (9,1)	242.76 (13,1)	248.66 (13,1)
15.0	359.50 (9,1)	369.75 (9,1)	237.58 (13,1)	243.38 (13,1)
100.0	346.15 (9,1)	355.55 (9,1)	228.27 (13,1)	233.93 (13,1)
$\gg 100.00$ (ceramic rich)	343.60 (9,1)	352.96 (9,1)	226.56 (13,1)	232.19 (13,1)

For the FGM shell of SUS304-Si_3N_4 and SUS304-Al_2O_3 the critical buckling temperatures are low when the FGM has only metallic material $\underline{n} = 0.0$; this does not hold true for the FGM of SUS304–ZrO_2. Here it is noticed that for the FGM shell with $\underline{n} = 100$ and $\underline{n} \gg 100.0$, the buckling temperatures are lower when compared to the case of $\underline{n} = 0.0$, i.e. metal rich. The change in the characteristics is mainly attributed to the coefficient of thermal expansion. The coefficient of thermal expansion is very high for both stainless steel (SUS304) and ZrO_2 when compared to Al_2O_3 and Si_3N_4. Further, the coefficient of thermal expansion for Zirconia (ZrO_2) is greater than that of stainless steel. Larger the coefficient of thermal expansion, lower the buckling temperature. For materials with a high coefficient of thermal expansion, considering uniform temperature rise, the strains due to temperature rise dominate the mechanical strains. Hence, the stresses due to temperature effects are larger when compared to the stresses from mechanical deflections. This

will lead to high initial compressive stresses in the FGM shell, which is likely to cause the shell to buckle at low thermal loading. In the latter case, the coefficient of thermal expansion α for alumina and silicon nitride are low when compared to SUS304 steel.

Other important observations from Tables 7–9 are the following: (i) When the thickness of the shell reduces the buckling temperature decreases as expected. (ii) With increase in l/r the buckling temperature increases for shells with $r/h = 100$ and 200. The ceramic materials, Si_3N_4 and Al_2O_3, in combination with SUS304 possess high buckling temperature when compared with FGM shell of SUS304–ZrO_2. For FGM shell with composition SUS304–ZrO_2, it is interesting to note that the buckling temperature decreases with increase in $\underline{n}$, with the exception of $\underline{n} = 1.0$, which breaks the continuity in decreasing trend. When considering the ceramics like Si_3N_4 and Al_2O_3, in combination with SUS304, the FGM shells are best suited for higher operating temperature since these exhibit high buckling temperature.

Results of similar studies are presented for FGMs composed of Ti–6Al–4V in combination with Si_3N_4, ZrO_2 and Al_2O_3 in Tables 10–12. Interesting observations on the buckling temperature are listed as follows: (i) from the viewpoint of constituent material composition, it is seen that for FGM shells with titanium alloy and silicon nitride and alumina, the buckling temperatures are low when the FGM is purely metallic and buckling temperature is very high when the FGM is composed of only ceramic. This observation is not true for the FGM of titanium alloy and zirconia. (ii) For FGMs of titanium alloy with alumina and silicon nitride the buckling temperature increases with an increase in the power-law index, whereas for FGMs of titanium alloy and zirconia, the buckling temperatures decrease with an increase in the power-law index. (iii) Certain exception on the influence of the power-law index on the buckling temperature may be noted in the case of FGMs of Ti–6Al–4V and Al_2O_3; when $\underline{n} = 0.05$ and 0.1 the buckling temperatures are low compared to FGMs with $\underline{n} = 0.0$ and 0.5 to $\gg 100.0$. (iv) From the viewpoint of geometry of the shell, for a given r/h (either 100 or 200), the buckling temperature increases with increase in l/r. For the shell with $r/h = 200$, the buckling temperatures are lower when compared to the shell with $r/h = 100$. These observations are similar to those described for FGM shell of stainless steel with ceramics. The circumferential mode number associated with critical buckling temperatures changes when r/h varies. But the mode number does not change with an increase in l/r for a given r/h.

3.7. Critical thermal buckling temperature based on average coefficient of thermal expansion

The objective of this section is to look for an alternate procedure for the determination of critical buckling temperature for FGM shells manufactured with various power-law indexes $\underline{n}$. In general, it is easy to obtain the critical buckling temperature of the homogeneous isotropic ceramic or metallic FGM shell. Following the assumptions that (i) geometrical parameters of the FGM shell and isotropic shell are the same, (ii) for a given geometry, thermal strains at the critical buckling temperature remain the same for the FGM shell and the isotropic shell and (iii) knowing the critical buckling temperature of the isotropic shell referred to as reference temperature, a method is proposed to evaluate the bifurcation buckling temperature of an FGM shell for a given $\underline{n}$. Since an FGM shell is assumed to consist of many homogeneous isotropic lamina, the coefficient of the thermal expansion of the FGM shell for a given power-law index is assumed to be equivalent to the average of the effective coefficient of thermal expansion of all layers and

Table 13
Comparison of the buckling temperature based on average coefficient of thermal expansion and iterative computational procedure for SUS304/Al_2O_3 FGM shell with $r/h = 100$ and $l/r = 1.0438$. ΔT_{ref} is of ceramic

$\underline{n}$	Based on actual computational procedure	Based on average coefficient of thermal expansion	%age difference
0.0	598.98	479.83	19.89
0.05	581.98	484.55	16.74
0.10	579.91	493.85	14.84
0.50	637.58	583.51	8.48
1.00	714.62	679.79	4.87
5.00	994.02	1015.86	−2.19
10.0	1106.30	1131.04	−2.23
15.0	1158.08	1177.36	−1.66
100.0	1265.14	1265.36	−0.017
$\gg 100.0$	1271.07	1271.06	−0.00079

coefficient of thermal expansion of each layer computed based on Eq. (4e). Then

$$\varepsilon^{\text{th}}\big|_{\underline{n}\gg 100.0} = \varepsilon^{\text{th}}\big|_{0.0\leqslant \underline{n}\leqslant 100.0} \quad \text{or} \quad (\alpha_{\text{ref}}\Delta T_{\text{ref}})_{\underline{n}\gg 100.0} = (\alpha_{\text{avg}}\Delta T_{\text{cri}})_{0.0\leqslant \underline{n}\leqslant 100.0}.$$

With the above relation the evaluation of the critical buckling temperature for a given value of the power-law index $\underline{n}$ is investigated. The left-hand side of the above equation represents the critical thermal strain of a homogeneous isotropic material, ceramic or metallic, which is equivalent to an FGM shell with $\underline{n} \gg 100.0$ or $\underline{n} = 0.0$; α_{ref} is the coefficient of thermal expansion of the isotropic shell and ΔT_{ref} refers to the reference temperature, which is equal to the critical buckling temperature for the isotropic shell. Given the critical buckling temperature for a homogeneous isotropic shell, and evaluating the average coefficient of thermal expansion α_{avg} for a given power-law index say, $\underline{n} = 0.05$ or 0.1 and so on, the above relation will yield the critical buckling temperature for the FGM shell corresponding to the choice of $\underline{n}$. The above procedure is implemented for the case of FGM shells composed of SUS304–Al_2O_3, $l/r = 1.0438$ and $r/h = 100$. Typical results for SUS304–Al_2O_3 FGM shells are listed in Tables 13 and 14 along with the percentage difference in the estimation of the critical buckling temperature by the alternate procedure.

It is to be noted that the buckling temperatures evaluated by this procedure depend on the reference temperature chosen as well as $\underline{n}$. This procedure can be used for the estimation of the critical buckling temperature during the preliminary design stage of an FGM shell. Thus, initially this helps in making a proper choice of the power-law index for the FGM shell, and subsequently the iterative procedure can be used to determine the actual buckling temperature.

4. Free vibration studies on FGM cylindrical shells

Free vibration natural frequency characteristics are presented for clamped–clamped FGM shells with various values of the power-law index. Apart from the free vibration studies, the effect of temperature on the free vibration natural frequencies of FGM shells is also investigated.

Table 14
Comparison of buckling temperature based on average coefficient of thermal expansion and iterative computational procedure for SUS304/Al_2O_3 FGM shell with $r/h = 100$ and $l/r = 1.0438$. ΔT_{ref} is of metal

$\underline{n}$	Based on actual computational procedure	Based on average coefficient of thermal expansion	%age difference
0.0	598.98	598.97	0.0016
0.05	581.98	610.57	−4.912
0.10	579.91	624.06	−7.613
0.50	637.58	730.66	−14.59
1.00	714.62	835.77	−16.95
5.00	994.02	1170.55	−17.75
10.0	1106.30	1279.70	−15.67
15.0	1158.08	1324.16	−14.34
100.0	1265.14	1414.02	−11.76
$\gg 100.0$	1271.07	1420.33	−11.74

Table 15
Comparison of first axial mode natural frequencies (Hz) of stainless steel and zirconia FGM shell for simply supported boundary condition

Circumferential mode m	$\underline{n} = 10$			$\underline{n} = 1.0$		
	Ref. [25]	Present	% difference	Ref. [25]	Present	% difference
1	14.21	13.8	2.89	13.7	14.5	−5.84
2	5.076	4.7	7.41	4.97	4.9	1.41
3	4.67	4.3	7.92	4.264	4.6	−7.88
4	7.91	7.3	7.71	7.1	7.8	−9.86
5	12.18	11.7	3.94	11.67	12.4	−6.26
6	18.17	17.1	5.89	16.24	18.2	−12.07
7	24.16	23.6	2.32	22.84	25	−9.46
8	32.49	31	4.59	30.45	32.9	−8.05
9	40.61	39.4	2.98	37.9	41.8	−10.29
10	50.76	48.8	3.86	47.71	51.8	−8.57

4.1. *Validation of natural frequencies for functionally graded cylindrical shells*

The strain–displacement relations from Love's shell theory were used by Pradhan et al. [25] to study free vibration natural frequencies of FGM shells. The present work attempts to simulate few results based on the first-order shear deformation theory applicable for moderately thick shells. The cylindrical shell geometry considered for the study is as follows: $l/r = 20.0$, $h/r = 0.002$. The FGM cylindrical shell is composed of stainless steel and zirconia. Various values of the power-law index $\underline{n}$ were used in the study, $\underline{n} = 0.0$ (metal rich, i.e. stainless steel), 0.1, 0.5, 1.0, 5.0, 10.0 and greater than 10.0 (FGM shell rich in zirconia). Table 15 gives a comparison of

Table 16
Comparison of natural frequencies (Hz) of stainless steel and zirconia FGM shell for clamped–clamped boundary condition

Circumferential mode m	$\underline{n} = 10$			$\underline{n} = 1.0$		
	Ref. [25]	Present	% difference	Ref. [25]	Present	% difference
1	30.45	28.6	6.08	29.44	29.6	−0.54
2	10.66	10.1	5.25	10.15	10.5	−3.45
3	6.1	6.2	−1.64	6.09	6.4	−5.09
4	7.92	7.8	1.52	7.41	8.2	−10.66
5	12.2	12	1.64	11.67	12.5	−7.11
6	17.77	17.4	2.08	16.75	18.2	−8.66
7	24.36	23.9	1.89	23.04	25	−8.51
8	32.5	31.4	3.38	30.45	32.9	−8.05
9	40.6	40	1.48	39	41.8	−7.18
10	50.77	49.5	2.5	48.73	51.8	−6.3

the natural frequencies for simply supported FGM cylindrical shells for the power-law indexes 10 and 0.1. Likewise, Table 16 lists the natural frequencies for the clamped–clamped FGM cylindrical shell. In general, it is observed that the frequency characteristics determined from Love's Theory of Shells and first-order shear deformation theory for the general shell of revolution, fairly agree with each other.

4.2. Natural frequency of FGM cylindrical shells without temperature effects

FGM shells composed of SUS304 stainless steel in combination with silicon nitride and titanium alloy with aluminium oxide have been chosen for the free vibration studies. The first axial mode frequencies associated with first 20 circumferential modes for a clamped–clamped boundary condition are presented in Figs. 5(a) and (b) and Figs. 6(a) and (b). The shell geometry is typically a long shell, $l/r = 5.21$, and the thickness of the shell follows from the following radius to thickness ratios: $r/h = 100$ and 200. The frequency characteristic is typical of homogeneous isotropic or orthotropic shells, depicting a bathtub curve. The frequency characteristics do not change irrespective of the power-law index. The influence of the power-law index is mainly to change the magnitude of the first axial mode frequencies. As the power-law index increases, the frequencies increase. The frequencies are low for power-law index $\underline{n} = 0.0$ and high for $\underline{n} >= 100$. This is expected because Young's modulus of ceramics, Si_3N_4 and Al_2O_3, are much higher compared to their metal counterpart. The power-law index does not have great influence in shifting the associated circumferential mode number for the lowest of the first axial mode frequencies. But, however, the change in the thickness of the FGM shell does alter the mode number of the lowest natural frequency. Thus, for FGM shell of SUS304/Si_3N_4, $r/h = 100$ the mode number of the lowest natural frequency is (4,1) and for $r/h = 200$ the mode number of the lowest natural frequency is (5,1). This holds true for the FGM shell of Ti–6Al–4V/Al_2O_3.

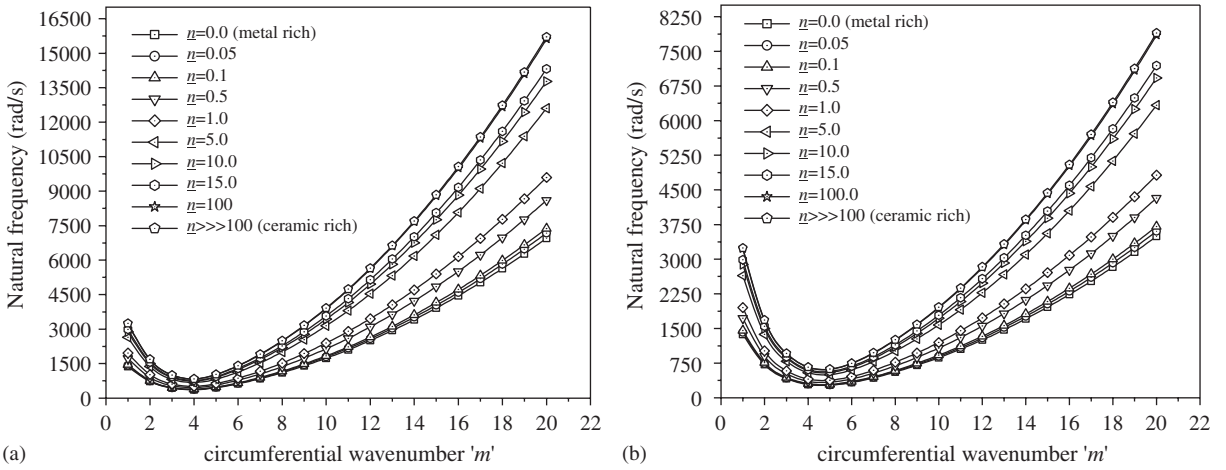

Fig. 5. Free vibration frequency of SUS304/Si_3N_4 FGM cylindrical shell. $l/r = 5.21$, and clamped–clamped boundary condition. (a) $r/h = 100$; lowest natural frequency mode (4,1). (b) $r/h = 200$; lowest natural frequency mode number (5,1).

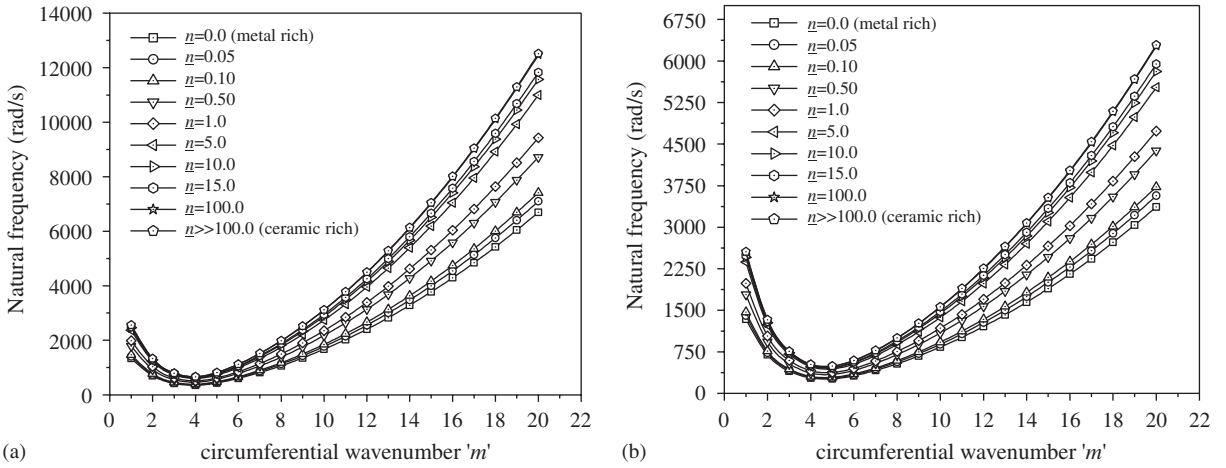

Fig. 6. Free vibration natural frequency characteristics of Ti–6Al–4V/Al_2O_3 FGM cylindrical shell. $l/r = 5.21$ and clamped–clamped boundary condition. (a) $r/h = 100$; lowest natural frequency is associated with (4,1). (b) $r/h = 200$; lowest natural frequency is associated with (5,1).

4.3. Effect of temperature on the free vibration frequency of FGM cylindrical shells

To understand the behavior of the natural frequency variation with respect to temperature, studies have been carried out on SUS304–Si_3N_4 and Ti–6Al–4V–Al_2O_3 FGM cylindrical shells. The FGM shells are ceramic rich on the inner surface. This configuration is best suited for shells conveying fluids at high temperature. The evaluation of the natural frequencies is conducted based on the specified temperature on the inner surface and the outer surface is always at ambient

temperature. The temperature on the inner surface is varied in steps of suitable increments and the highest temperature for the study is limited to the critical buckling temperature for the shell geometry and FGM composition (or power-law index $\underline{n}$). The lowest buckling temperature for SUS304–Si_3N_4 FGM shell with a geometry of $l/r = 5.21$ and $r/h = 100$ and 200 for various power-law indexes is listed in Table 7 and for the FGM shell of Ti–6Al–4V–Al_2O_3 in Table 11. Now, given the temperature boundary condition on the inner surface and ambient temperature on the outer surface, the converged temperature distribution is obtained. Based on the converged temperature distribution, the thermal load vector, total initial stresses and hence the geometric stiffness matrix are computed. This initial stiffness matrix is added to the stiffness matrix of the FGM shell and along with the mass matrix, a system of second-order linear differential equations is solved for free vibration frequencies for various circumferential modes. Numerical results have been obtained for various modes (m,n) like (1,1), (4,1), (9,1), (10,1), (15,1) and (20,1) for SUS304–Si_3N_4 FGM shell with $l/r = 5.21$ and $r/h = 100$ and 200. Power-law indexes like $\underline{n} = 0.0$, 0.1, 1.0, 10.0 and $\gg 100.0$, which define the composition profiles, were used. Typical results are illustrated in Figs. 7(a)–(f) for SUS304–Si_3N_4 FGM shell with $l/r = 5.21$ and $r/h = 100$.

It is clear from Fig. 7 that the natural frequencies decrease with increase in temperature. From the free vibration studies it was noted that the natural frequencies are higher for higher values of the power-law index. Further, higher the power-law index, higher the buckling temperatures. Of course this depends on the constituent materials used for FGM. Further, the characteristic variation of the natural frequency with respect to temperature depends on the mode numbers. Referring to Figs. 7(a) and (f), for mode (1,1) and (20,1), respectively, it is seen that the fall in the natural frequency is not appreciable with increase in temperature. This is probably due to the membrane effects dominating the meridional stress resultants due to temperature rise for lower mode (1,1) (refer Fig. 5(a)). For higher mode (20,1) the bending strain energy dominates the meridional stress resultants. Similarly, for higher modes like (10,1) and (15,1) the negligible fall in frequency for the initial increase in temperature is to be noted (Figs. 7(d) and (e)). This can be attributed to the dominating influence of the bending strain energy and the effect of temperature rise is less. However, the sudden and gradual decrease in the natural frequencies for higher temperature may be noted where probably the meridional stress resultants overtake the effect of bending strain energy. For the mode like (4,1) (Fig. 7(b)), which corresponds to the lowest natural frequency of the shell (refer Fig. 5(a)), the membrane effect as well as the bending strain energy is minimal. Hence, the fall in frequency is smooth and gradual as the temperature increases and for temperature close to the buckling temperature, the frequencies take on very low values. Now consider mode (9,1) in Fig. 7(c). It is the mode corresponding to the lowest thermal buckling temperature. Hence, the meridional stress resultants are large and compressive in nature for a given rise in temperature. Also mode (9,1) is associated with reasonably high bending strain energy (refer Fig. 5(a)). But the high meridional stress resultants dominate the bending strain energy and cause the fall in natural frequencies gradually and continuously as the temperature increases (Fig. 7(c)), similar to that observed in the case of mode (4,1). However, the magnitudes of the frequency are slightly higher compared to mode (4,1). Thus, it is clear that the effect of temperature is felt more for the modes corresponding to the lowest natural frequency and lowest thermal buckling temperature and more so for the lowest natural frequency mode.

Similar results were obtained for FGM shells of Ti–6Al–4V/Al_2O_3, $l/r = 5.21$ and $r/h = 100$ and 200. Typical results for the variation of natural frequencies for Ti–6Al–4V/Al_2O_3, $l/r = 5.21$

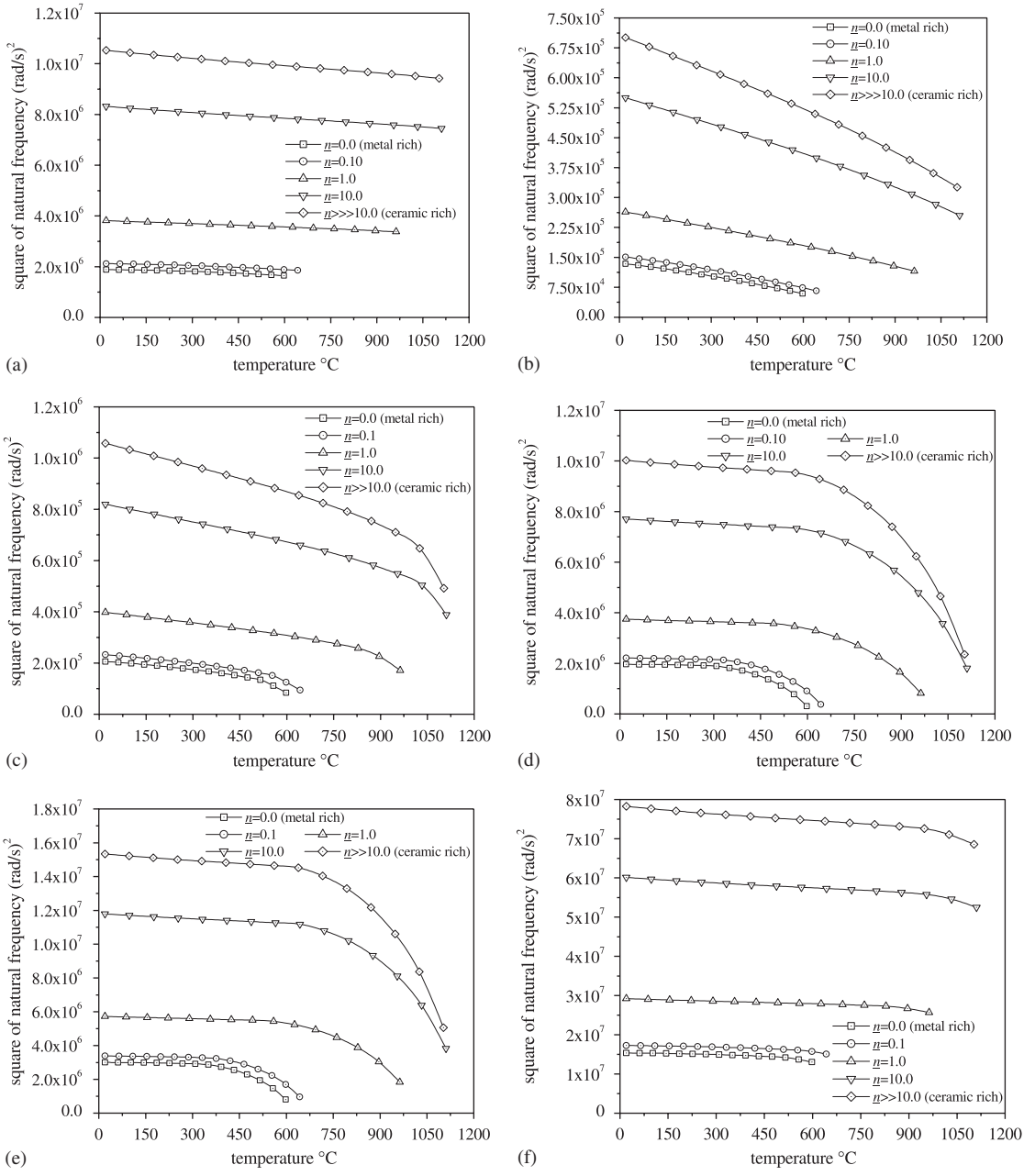

Fig. 7. Effect of temperature on the free vibration frequencies of SUS304/Si_3N_4 FGM cylindrical shell. $l/r = 5.21$, $r/h = 100$ and clamped–clamped boundary condition.

and $r/h = 200$ are illustrated in Figs. 8(a)–(f) and are now considered for discussion. Here, results are presented for modes (4,1) and (5,1), which correspond to the lowest natural frequency of the shell. The smooth, gradual and continuous fall in the natural frequencies may be noted (Figs. 8(b)

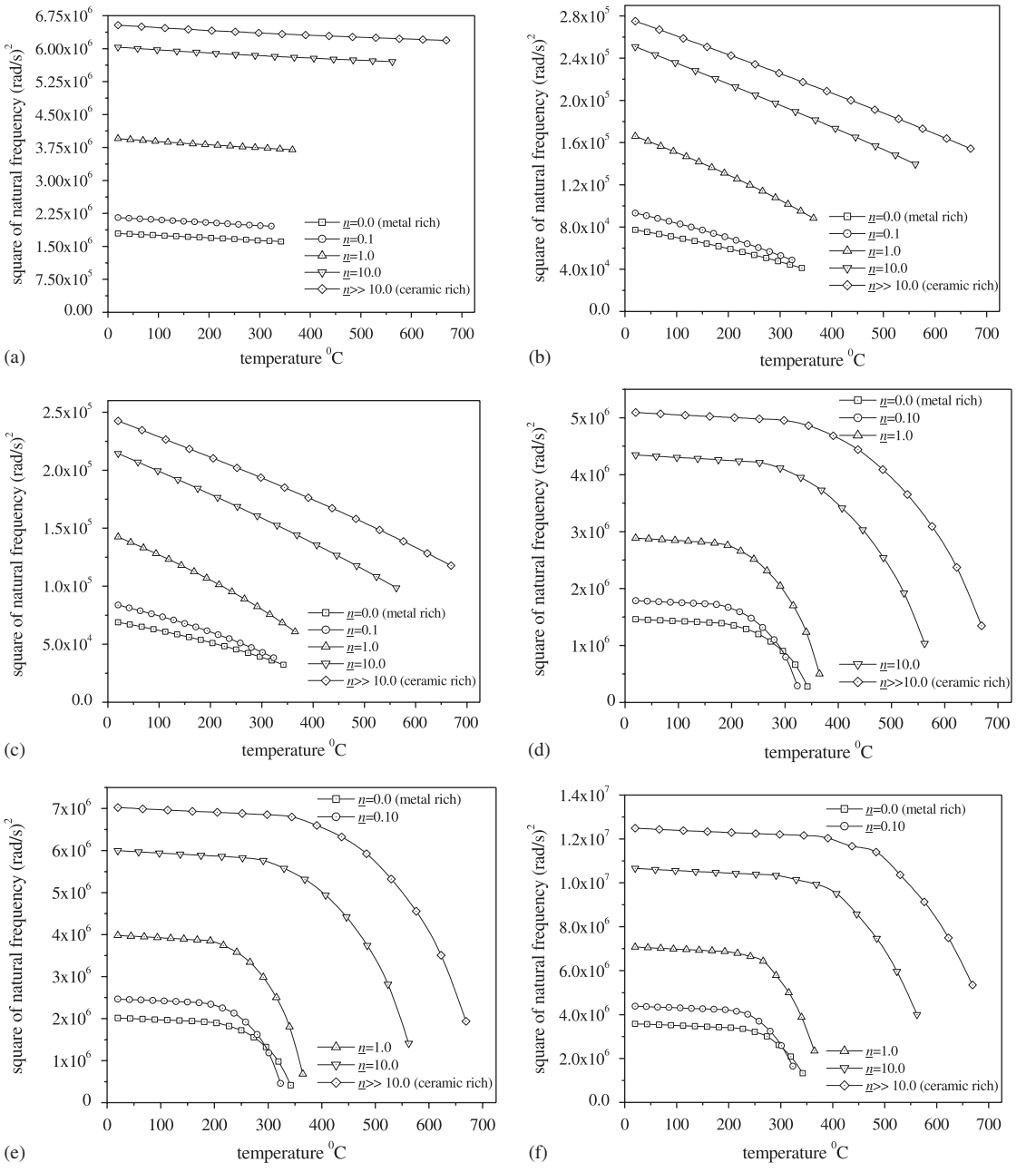

Fig. 8. Effect of temperature on FGM cylindrical shell Ti–6Al–4V/Al_2O_3. $l/r = 5.21$, $r/h = 200$ and clamped–clamped boundary condition.

and (c)) as the temperature increases. The lowest buckling temperature mode is (13,1) and also another mode close to this is (12,1). For these modes, the variation of the natural frequencies with respect to temperatures is presented in Figs. 8(d) and (e). For modes (13,1) and (12,1), the

meridional stress resultants are high. Referring to Fig. 6(b), the modes (12,1) and (13,1) are on the higher circumferential mode side where the bending strain energy dominates. Hence, for initial rise in temperature the bending strain energy probably dominates the meridional stress resultants due to temperature rise. However, for higher temperatures and temperatures close to the buckling temperature, the magnitude of the meridional stress resultants overtake bending strain energy and cause the frequencies to fall drastically (Figs. 8(d) and (e)).

5. Conclusions

A theoretical analysis on thermal buckling and free vibration of functionally graded cylindrical shells using semianalytical finite element based on first-order shear deformation theory was presented. Important conclusions from the numerical analysis are summarized as follows. The magnitude of the lowest buckling temperature greatly depends on the composition of the metal–ceramic constituents. FGM shell of SUS304–Si_3N_4, Ti–6Al–4V–Si_3N_4, SUS304–Al_2O_3 and Ti–6Al–4V–Al_2O_3 have high buckling temperature when compared to FGM shells of SUS304–zirconia and Ti–6Al–4V–zirconia constituents. The power-law index is shown to influence the buckling temperature. For FGMs containing ceramics like Si_3N_4 and Al_2O_3 in combination with metal, the buckling temperature increases with increase in the power-law index (i.e. FGM rich in ceramic when compared to metal). However, for FGMs with metal and zirconia as ceramic, the buckling temperature decreases with increase in the power-law index. In other words, the thermal buckling temperature mainly depends on the coefficient of thermal expansion of the constituent materials. Materials with lower coefficient of thermal expansion will have high thermal buckling temperature. The lowest buckling temperature mode does not change for a shell of given geometry as the power-law index changes. For FGM shells with $r/h = 100$ and 200, the buckling temperature increases with increase in l/r. Free vibration natural frequency characteristics of FGM shells are similar to those of the isotropic shells. The lowest natural frequency mode does not change as the power-law index changes for a clamped–clamped cylindrical shell. When temperature gradient exists along the shell wall, the fall in natural frequency is more apparent for the lowest natural frequency mode when compared to the mode with the lowest buckling temperature.

References

[1] N. Noda, Thermal stresses in functionally graded materials, *Journal of Thermal Stresses* 22 (1999) 477–512.
[2] T. Fuchiyama, N. Noda, Analysis of thermal stress in a plate of functionally gradient material, *JSAE Review* 16 (1995) 263–268.
[3] Y. Obata, N. Noda, Steady thermal stresses in a hollow circular cylinder and hollow sphere of a functionally gradient material, *Journal of Thermal Stresses* 17 (1994) 471–487.
[4] J.N. Reddy, C.D. Chin, Thermomechanical analysis of functionally graded cylinders and plates, *Journal of Thermal Stresses* 21 (1998) 593–626.
[5] M. Jabbari, S. Sohrabpour, M.R. Eslami, Mechanical and thermal stresses in a functionally graded hollow cylinder due to radially symmetric load, *International Journal of Pressure Vessels and Piping* 79 (2002) 493–497.

[6] H. Awaji, R. Sivakumar, Temperature and stress distribution in a hollow cylinder of functionally graded material: the case of temperature-independent material properties, *Journal of the American Ceramic Society* 84 (2001) 1059–1065.
[7] S. Takezono, K. Tao, E. Inamura, M. Inoue, Thermal stress and deformation in functionally graded material shells of revolution under thermal loading due to fluid, *JSME International Journal Series A* 39 (1996) 573–581.
[8] G.R. Ye, W.Q. Chen, J.B. Cai, A uniformly heated functionally graded cylindrical shell with transverse isotropy, *Mechanics Research Communications* 28 (2001) 535–542.
[9] K.M. Liew, S. Kitipornchai, X.Z. Zhang, C.W. Lim, Analysis of the thermal stress behavior of functionally graded hollow circular cylinders, *International Journal of Solids and Structures* 40 (2003) 2355–2380.
[10] J.R. Cho, D.Y. Ha, Volume fraction optimization for minimizing thermal stress in Ni–Al_2O_3 functionally graded materials, *Materials Science and Engineering A* 334 (2002) 147–155.
[11] Y. Ootao, Y. Tanigawa, T. Nakamura, Optimization of material composition of FGM hollow circular cylinder under thermal loading: a neural network approach, *Composites Part B* 30 (1999) 415–422.
[12] X.Q. He, T.Y. Ng, S. Sivashanker, K.M. Liew, Active control of FGM with integrated piezoelectric sensors and actuators, *International Journal of Solids and Structures* 38 (2001) 1641–1655.
[13] T.Y. Ng, X.Q. He, K.M. Liew, Finite element modeling of active control of functionally graded shells in frequency domain via piezoelectric sensors and actuators, *Computational Mechanics* 26 (2002) 1–9.
[14] K.M. Liew, H. K Lim, M.J. Tan, X.Q. He, Analysis of laminated composite beams and plates with piezoelectric patches using the element-free Galerkin method, *Computational Mechanics* 29 (2002) 486–497.
[15] K.M. Liew, X.Q. He, T.Y. Ng, S. Sivashanker, Active control of FGM plates subjected to a temperature gradient; modelling via. Finite element method based on FSDT, *International Journal of Numerical Methods in Engineering* 52 (2001) 1253–1271.
[16] K.M. Liew, X.Q. He, T.Y. Ng, S. Kitipornchai, Active control of FGM shells subjected to a temperature gradient via piezoelectric sensor/actuator patches, *International Journal of Numerical Methods in Engineering* 55 (2002) 653–668.
[17] K.M. Liew, J. Yang, S. Kitipornchai, Postbuckling of piezoelectric FGM plates subject to thermo-electro-mechanical loading, *International Journal of Solids and Structures* 40 (2003) 3869–3892.
[18] S. Kitipornchai, J. Yang, K.M. Liew, Semi-analytical solution for nonlinear vibration of laminated FGM plates with geometric imperfections, *International Journal of Solids and Structures* 41 (2004) 2235–2257.
[19] J. Yang, S. Kitipornchai, K.M. Liew, Large amplitude vibration of thermo-electro-mechanically stressed FGM laminated plates, *Computer Methods in Applied Mechanics and Engineering* 192 (2003) 3861–3885.
[20] J. Yang, K.M. Liew, S. Kitipornchai, Dynamic stability of laminated FGM plates based on higher-order shear deformation theory, *Computational Mechanics* 33 (2004) 305–315.
[21] R. Shahsiah, M.R. Eslami, Thermal buckling of functionally graded cylindrical shell, *Journal of Thermal Stresses* 26 (2003) 277–294.
[22] H.S. Shen, Postbuckling analysis of axially-loaded functionally graded cylindrical shells in thermal environments, *Composite Science and Technology* 62 (2002) 977–987.
[23] H.S. Shen, Postbuckling analysis of pressure-loaded functionally graded cylindrical shells in thermal environments, *Engineering Structures* 25 (2003) 487–497.
[24] C.T. Loy, K.Y. Lam, J.N. Reddy, Vibration of functionally graded cylindrical shells, *International Journal of Mechanical Sciences* 41 (1999) 309–324.
[25] S.C. Pradhan, C.T. Loy, K.Y. Lam, J.N. Reddy, Vibration characteristics of functionally graded cylindrical shells under various boundary conditions, *Applied Acoustics* 61 (2000) 111–129.
[26] L.W. Chen, L.Y. Chen, Thermal buckling behavior of laminated composite plates with temperature-dependent properties, *Composite Structures* 13 (1989) 275–287.
[27] M. Taya, R.J. Arsenault, *Metal Matrix Composites Thermomechanical Behavior*, Pergamon Press, England, 1989.
[28] L. Banks-Sills, R. Eliasi, Y. Berlin, Modeling of functionally graded materials in dynamic analyses, *Composites: Part B Engineering* 33 (2002) 7–15.
[29] Y. Tanigawa, Some basic thermoelastic problems for nonhomogeneous structural materials, *Applied Mechanics Review* 48 (1995) 287–300.

[30] N. Ganesan, R. Kadoli, Buckling and dynamic analysis of piezothermoelastic composite cylindrical shell, *Composite Structures* 59 (1) (2003) 45–60.
[31] O.C. Zienkiewicz, R.L. Taylor, *The Finite Element Method*, vol. 2, *Solids and Fluid Mechanics*, *Dynamics and Non-Linearity*, fourth ed., McGraw-Hill, Singapore, 1991.
[32] C.T.F. Ross, *Pressure Vessels under External Pressure: Statics and Dynamics*, Elsevier Applied Science, London, 1994.
[33] R.D. Cook, D.S. Malkus, M.E. Plesha, *Concepts and Applications of Finite Element Analysis*, third ed., Wiley, Singapore, 2000.
[34] J.N. Reddy, *An Introduction to the Finite Element Method*, McGraw-Hill International Editions, Singapore, 1984.
[35] R.K. Thangaratnam, Palaninathan, J. Ramachandran, Buckling of composite cylindrical shells, *Journal of the Aeronautic Society of India* 41 (1989) 47–54.
[36] G.N. Praveen, C.D. Chin, J.N. Reddy, Thermoelastic analysis of functionally graded ceramic–metal cylinder, *Journal of Engineering Mechanics* 125 (1999) 1259–1267.
[37] S.S. Rao, *The Finite Element Method in Engineering*, third ed., Butterworth Heinemann, New Delhi, 1999.
[38] L.J. Segerlind, *Applied Finite Element Analysis*, second ed., Wiley, New York, 1984.